

Diffraction and microscopy with attosecond electron pulse trains

Yuya Morimoto^{1,2} and Peter Baum^{1,2*}

Attosecond spectroscopy¹⁻⁷ can resolve electronic processes directly in time, but a movie-like space-time recording is impeded by the too long wavelength (~100 times larger than atomic distances) or the source-sample entanglement in re-collision techniques⁸⁻¹¹. Here we advance attosecond metrology to picometre wavelength and sub-atomic resolution by using free-space electrons instead of higher-harmonic photons¹⁻⁷ or re-colliding wavepackets⁸⁻¹¹. A beam of 70-keV electrons at 4.5-pm de Broglie wavelength is modulated by the electric field of laser cycles into a sequence of electron pulses with sub-optical-cycle duration. Time-resolved diffraction from crystalline silicon reveals a <10-as delay of Bragg emission and demonstrates the possibility of analytic attosecond-ångström diffraction. Real-space electron microscopy visualizes with sub-light-cycle resolution how an optical wave propagates in space and time. This unification of attosecond science with electron microscopy and diffraction enables space-time imaging of light-driven processes in the entire range of sample morphologies that electron microscopy can access.

Our concepts for generating attosecond electron pulses, direct streaking-oscilloscope characterization, atomic diffraction and proof-of-principle attosecond electron microscopy of electromagnetic fields are depicted in Fig. 1. A femtosecond laser¹² triggers electron emission from a photocathode (yellow) and produces electron pulses of ~1 ps duration at a central energy of $E_{el} = 70$ keV (ref. ¹³). The de Broglie wavelength is $\lambda_{el} \approx 4.5$ pm and space-charge effects are avoided by using fewer than one electron per pulse at the sample. A first laser beam ('modulation') is used to compress the electron pulse into a sub-cycle pulse train. For this purpose, we let the laser beam and the electron beam intersect at a 50-nm-thick silicon nitride membrane that lets the electrons pass through. The membrane is also transparent to the laser beam (1,030 nm wavelength), but the refractive index of ~2 in combination with thin-layer interferences generates a phase shift between the incoming and outgoing electromagnetic waves. Therefore, the periodic electromagnetic acceleration and deceleration of the propagating electrons in the optical field cycles before and after the membrane do not cancel out after passage through the laser focus, as would happen in free space¹³. In the end, there remains a time-dependent overall momentum kick that is proportional to the change of vector potential at the membrane and therefore dependent on the optical phase. In contrast to metal foils^{13,14}, graphite¹⁵ or nanostructures¹⁶, a dielectric membrane has negligible linear or nonlinear optical absorption and can therefore sustain an extreme level of power and fields, enabling strong/effective compression and metrology.

In the experiment, we let the electron beam (0.48× speed of light) and the laser beam (p-polarized, ~15 mW, peak field $\sim 5 \times 10^7$ V m⁻¹) hit the membrane under 35° and 60° from the surface normal, respectively. In this geometry (close to Brewster's angle), there is predominantly a periodic acceleration and deceleration of the electrons that is dependent on the arrival time at the membrane with respect to the laser cycles. Calculations predict¹⁷⁻¹⁹ that such a periodic energy modulation¹⁹ can reshape the incoming electron packet after some free-space propagation into a train of attosecond pulses^{15,18-20} (see Fig. 1). A homogeneous compression of the entire electron beam (diameter 135 μm) is achieved by setting the optical focus larger (diameter ~300 μm) and the pulses longer in time (~1.7 ps). For temporal pulse characterization, we apply at 3.7 mm distance a second dielectric membrane (60 nm of silicon) and a second laser beam ('excitation' in Fig. 1). The optical peak field at the silicon membrane is several times higher ($\sim 2 \times 10^8$ V m⁻¹) and the foil's refractive index is greater (~3.5). Therefore, the previously negligible sideways forces are now substantial and create a time-dependent beam deflection; that is, a cathode ray oscilloscope at optical frequencies (petahertz). Further modulations in time are now irrelevant. As the sub-cycle electron pulse train generated at the first membrane is temporally synchronized to the characterization laser's optical cycles¹⁷, each attosecond electron pulse in the pulse train sees the same kind of deflection dynamics, and a time-integrated measurement characterizes the average pulse duration and shape¹.

Figure 2a shows the electron beam shape when all lasers are off. Figure 2b depicts the beam when the characterization oscilloscope ('excitation' in Fig. 1) is activated. We observe an elongated spot with two maxima at the ends (Fig. 2b), which can be identified as the turning points of the periodic deflection at the optical frequency. We infer a streaking speed of ~ 0.2 mrad fs⁻¹, which is ~25 times faster than previously achieved with terahertz radiation¹³. When the compression laser is also activated and adjusted to proper field strength, the streak of Fig. 2b turns into a localized spot that moves up and down with a sinusoidal dependence on the optical phase delay between the two laser beams (see Fig. 2c). This real-space streaking result directly demonstrates, in probably the clearest possible way, the presence of electron pulses with sub-optical-cycle localization in time^{15,18-20}.

The duration of the laser-compressed electron pulses can be inferred from the streaked spot width divided by the streaking speed¹³, but numerically fitting the entire deflectogram to a model is more accurate. We assume a Gaussian electron pulse shape of width τ_{el} on top of a time-independent background originating from uncompressed electrons from the non-converging optical cycles¹⁷. The deflection is modelled by a sinusoidal oscillation with

¹Ludwig-Maximilians-Universität München, Am Coulombwall 1, 85748 Garching, Germany. ²Max-Planck-Institute of Quantum Optics, Hans-Kopfermann-Str. 1, 85748 Garching, Germany. *e-mail: peter.baum@lmu.de

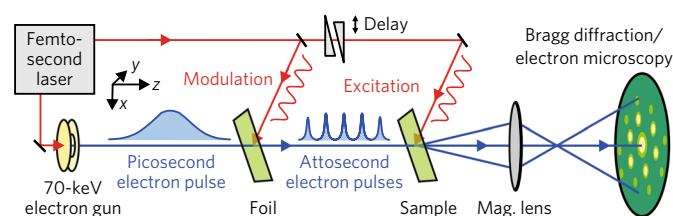


Fig. 1 | Concept and experiment. A photo-emitted picosecond electron pulse (blue) with a sub-atomic de Broglie wavelength is temporally modulated at a dielectric foil (green) by the optical cycles of a femtosecond laser (red) into a train of attosecond electron pulses (blue). Electron diffraction from a cycle-excited sample (green) can produce atomic resolution in space and time. Alternatively, real-space electron microscopy can reveal optical near-field vectors and phase delays with sub-cycle time resolution.

free amplitude and phase at the fixed laser-cycle period of 3.44 fs. Optimization of these four parameters results in the blue lines in Fig. 2d, in noteworthy agreement with the experiment (dots). Figure 2e shows the electron pulse shape in time and reveals a pulse duration (above the background) of 0.35 fs root-mean-square or 0.82 fs full-width-at-half-maximum. These values are upper limits, because potential short-time interferometric instabilities in the experiment cannot entirely be excluded. Fig. 2f shows the electron pulse duration as a function of the compression laser's peak field strength, showing a characteristic shortening (compression) and subsequently an increase (over-compression) of the pulse width^{13,21}. The best-compressed electron pulses in the train are about 35 times shorter than previously reported for atomic-resolution diffraction²¹.

Beam quality is not substantially altered by the compression. Figure 2g reports magnetic waist scans as a measurement of emittance; that is, a product of beam size and divergence. The beam's transverse and longitudinal coherence lengths, which define an electron's ability to interfere with itself when diffracted from a complex material, are directly related²². In the y direction (perpendicular to the laser polarization), there is no measurable change of emittance ($\epsilon_{ps}^y \approx \epsilon_{as}^y \approx 0.94$ nm), and in the x direction, we observe a slight increase from $\epsilon_{ps}^x \approx 0.85$ nm to $\epsilon_{as}^x \approx 1.37$ nm. This difference originates from tiny sideways deflections at the compressor stage in combination with a non-perfectly collimated electron beam there, an effect that can be avoided at appropriate incidence angles (see Fig. 2h). With $\epsilon_{as}^x \approx 1.37$ nm, the predicted transverse coherence for a beam with radius $\sigma_x \approx 100$ μ m is $\lambda_{el}\sigma_x/(2\pi\epsilon_{as}^x) \approx 50$ nm and therefore larger than a complex molecule or unit cell. Figure 3a shows the inner part of a diffraction pattern of 60-nm-thick single-crystalline silicon in the $[-1/\sqrt{2}, \sqrt{2}, 1/\sqrt{2}]$ direction, obtained with the attosecond electron pulses. Tens of Bragg spots are discernible and demonstrate the atomic resolution. Figure 3b shows the rocking curve (angle-dependent intensity) of the $1\bar{1}3$ spot, revealing a width that is limited by sample thickness (~ 70 nm in beam direction) and almost identical traces for uncompressed and compressed electron pulses. The asymmetry is a sign of substantial multiple-scattering interferences, but equally strong in both cases. The attosecond pulses do not obtain any substantial energy spread ΔE . The time-energy uncertainty principle and the measured Bragg spot width changes caused by the compression restrict ΔE to 4.5–60 eV and $\Delta E/E_{el}$ to 10^{-4} – 10^{-5} . This monochromaticity is ~ 100 times better than in high-harmonic pulses or re-colliding electrons and might be useful for attosecond electron energy-loss spectroscopy of, for example, inner-shell dynamics in atoms or some high-energy plasmonic processes. Figure 3c shows that the overall intensity of the Bragg spots (that is, the structure factor representing the scattering potential within the unit cell) does not change beyond the

experimental shot-noise limit when activating the compression. Diffractive imaging of laser-driven electronic motion in molecules or condensed matter requires percentage-level sensitivities to intensity changes^{23–26}, a signal-to-noise ratio that our attosecond electron pulses can provide (see Fig. 3c), even although our electron source was operated far from optimum conditions (see Methods). These results demonstrate that laser-compression of an electron beam into attosecond pulses does not substantially modify any spatial beam parameter; only the effective current is approximately halved by the presence of a constant background (see Fig. 2e) and further reduced by scattering and absorption at the compressor membrane. In summary, the experimental tools are now available for analytic attosecond-ångström diffraction with fundamental space–time resolution.

We report two proof-of-principle applications. Many photo-electric processes in atoms, molecules, solids or liquids occur with subtle delays on attosecond timescales^{7,27–31} that are related to tunnelling or propagation of quasi-free electrons in the potential or band structure of the material, modified by electron–electron interactions and screening. Here, we investigate whether Bragg diffraction (that is, the conversion of crystal momentum to electron momentum) takes time or not. The silicon membrane was oriented for diffraction and simultaneously laser-excited. In this geometry, the electromagnetic streaking dynamics of the attosecond electron wavepackets in the laser field before and after the foil superimposes with the Bragg condition inside the foil, causing diffraction and deflection in synchrony. All Bragg spots show a pronounced time-dependent streaking when scanning the laser phase delay (see Fig. 3d). A centre-of-mass analysis^{27,31} reveals any potential delays between a Bragg spot and the direct beam (000-spot) with extreme precision (see Fig. 3e). Figure 3f summarizes the results: electron-crystal scattering at tens of kiloelectronvolts occurs with no delay on attosecond timescales (< 40 as for every single Bragg spot, < 10 as root-mean-square for all eight spots). Multiple scattering, plasmonic losses, inner-shell processes, electron–electron exchange interactions or electromagnetic fields exceeding 10^8 V m⁻¹ or 0.3 T do not affect the attosecond-level timing with which Bragg electrons are emitted from a crystal.

In a second application, we invoke real-space electron microscopy and report a proof-of-principle demonstration at low magnification. While the motion of bound electrons occurs naturally on atomic dimensions, where diffraction is an applicable approach for imaging, collective carrier dynamics and transport often involve nanometre dimensions and above (for example, in metamaterials or biological/technological light–energy conversions). We illuminated a 130×150 - μ m big silicon membrane with the electron pulse train and adjusted the excitation laser slightly off-angle with the compression laser, in order to generate a travelling optical excitation wave on the sample. Figure 4a shows the membrane's static image and Fig. 4b reveals the time-dependent intensity changes observed with the attosecond pulses (see also Supplementary Movie 1). Fitting a temporal phase to each location reveals the delay map depicted in Fig. 4c, showing a continuous and substantial phase advance from left to right (x direction). Figure 4d illustrates the contrast mechanism: each point of the sample deflects the electron beam with a phase delay and amplitude that is determined by the optical waveform at that location. Deflection angles $\alpha(x, t)$ originating from the tilted incidence of the excitation wave can be convergent or divergent in x , leading to local intensity increases and decreases, which follow in space and time the travelling-wave propagation (see Fig. 4d). A condition for such combined spatial/angular imaging³² in the experiment is an out-of-focus magnification (see Fig. 4e); otherwise, any ray originating from a certain sample location would end up at the same detector position regardless of deflection. Integrating over $y = 20$ μ m reveals the space–time results of Fig. 4f in comparison with a simulation based on ray optics and $\alpha(x, t)$ from a travelling wave. While in the middle region the intensity is highest

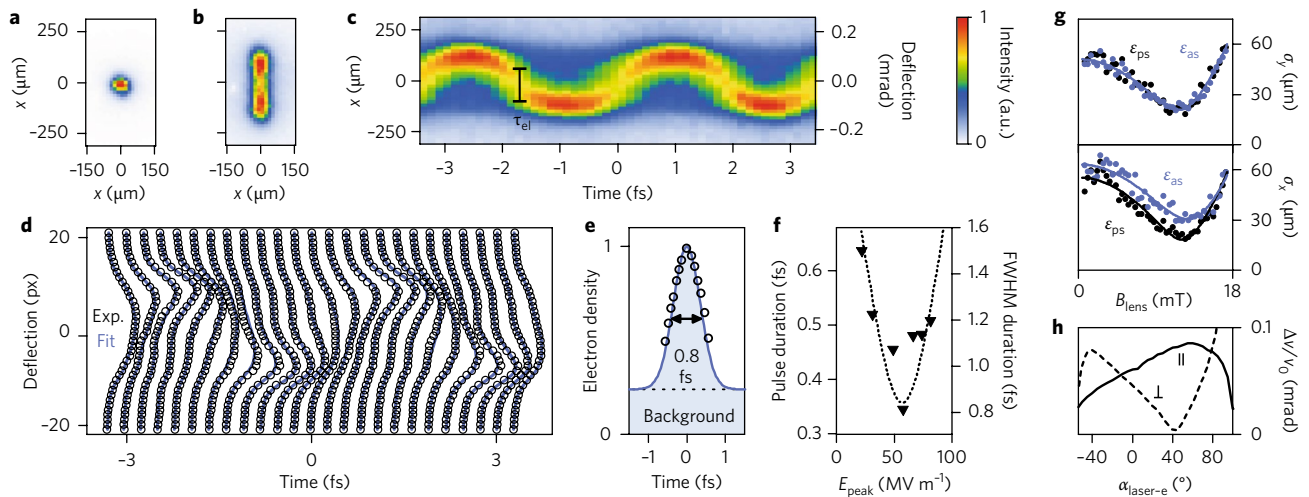


Fig. 2 | Attosecond electron pulses. **a**, Basic electron beam profile. **b**, Streaking deflection of long electron pulses by optical field cycles. **c**, Streaking deflection of laser-compressed electron pulses as a function of delay. The oscillatory shape demonstrates the presence of sub-optical-cycle electron pulses. The streaking widths at the zero-crossings indicate the pulse duration. **d**, Comparison of experiment (dots) and numerical simulation (blue lines). **e**, Electron pulse shape, evaluated directly from the raw data (dots) or via the simulation fit (blue). The electron pulse duration (above background) is 820 as (full-width, see black arrow) or 350 as (root-mean-square). **f**, Electron pulse duration as a function of the compression laser's peak field strength E_{peak} . **g**, Beam quality measurements (emittance) for picosecond pulses (black) in comparison with the attosecond pulse train (blue). **h**, Numerical simulation (finite-difference time-domain, Lumerical Inc.) of the compression efficiency (\parallel) and residual sideways deflection (\perp) as a function of the laser-electron angle ($\alpha_{\text{laser-e}}$) for a fixed electron-foil incidence of 35° and a peak field strength of 10^9 V m^{-1} . An angle of $\sim 40^\circ$ provides efficient compression without sideways deflection.

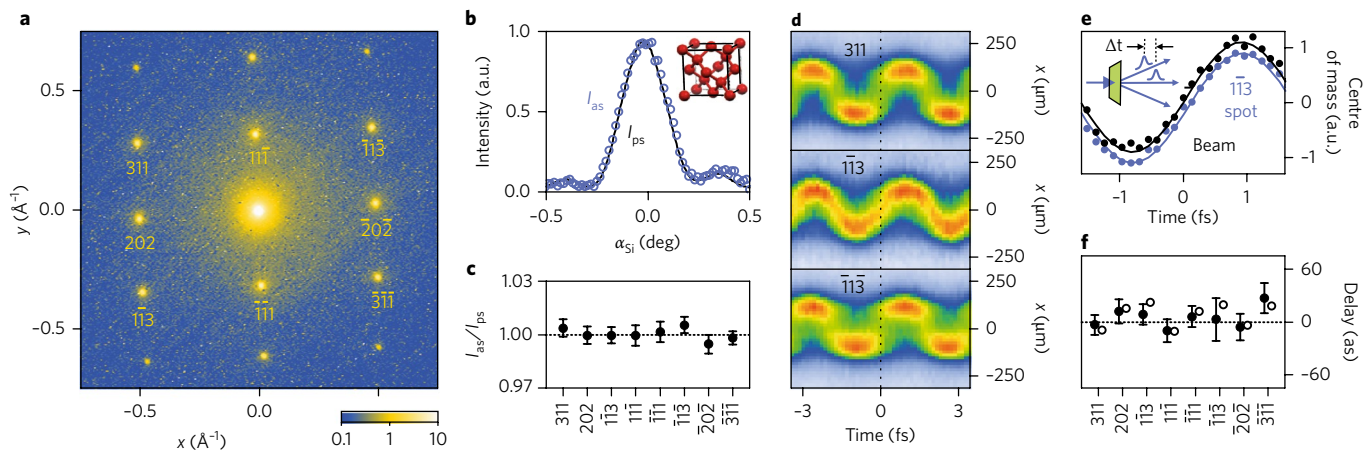


Fig. 3 | Atomic diffraction with attosecond electron pulses. **a**, Diffraction pattern of single-crystalline silicon, taken with the attosecond electron pulse train. The non-labelled Bragg spots are forbidden but visible via multiple scattering. **b**, Rocking curve of the $1\bar{1}3$ spot for picosecond pulses in comparison with the attosecond electron pulse train. Inset, crystal structure of silicon. **c**, Absolute intensity of all Bragg spots, measured with the attosecond pulses and normalized to the picosecond case. The error bars denote the shot noise of the measurement (~ 140 s integration). **d**, Streaking deflectograms of three example Bragg spots; all of them behave similarly. **e**, Centre-of-mass of the deflectogram of the $1\bar{1}3$ spot versus the direct beam for delay analysis. Inset, illustration of delays in Bragg spot emission. **f**, Measured attosecond-level delay of different Bragg spot emissions with respect to the direct beam. The filled and open circles are the results of centre-of-mass analysis and deflectogram fitting, respectively. The error bars represent standard deviation. The average delay is (4.6 ± 5.4) as.

at times where $d\alpha/dx$ is maximum (converging rays, see Fig. 4d), the highest or lowest intensities are observed at the membrane edges ($\pm 64 \mu\text{m}$) at times where α is highest or lowest, respectively. Indeed, the phase shift of the edge features is close to $\pi/2$ (see Fig. 4f, right panel). Figure 4g shows the y -integrated phases along x , revealing the travelling-wave parameter ($12 \text{ as } \mu\text{m}^{-1}$), the phase shift at the edges and a ~ 10 -as accuracy of this proof-of-principle microscopy experiment. State-of-the-art instrumentation¹⁹ and appropriate waveform electron microscopy³² with our attosecond pulses will

reveal nanoscale and potentially smaller electric and magnetic near-fields with spatial, temporal and vectorial resolution, hence the entire nanophotonic information.

Electron pulses at tens or hundreds of kiloelectronvolts can, in principle, have multi-kiloelectronvolt bandwidths and therefore zeptosecond duration. In our experiment, the degree of compression is limited by the available peak field strength at the compression membrane, by the distance to the sample, by the nonlinear shape of the optical cycles and by the uncorrelated energy spread

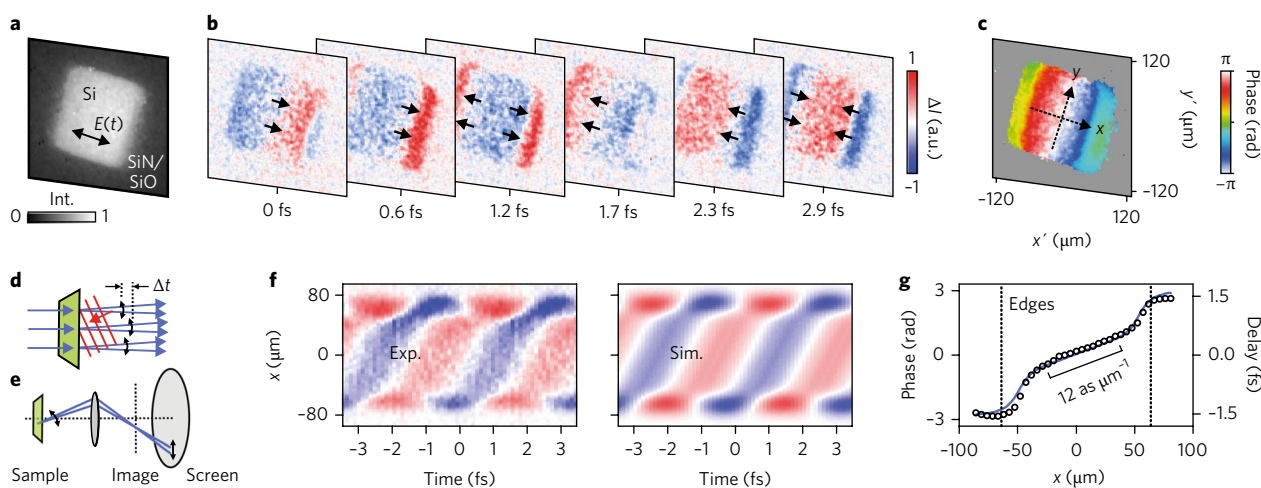


Fig. 4 | Attosecond electron microscopy of electromagnetic waveform propagation. **a**, Shadow image of a 60-nm-thick silicon membrane (grey) with SiN/SiO overcoat (black) at low magnification. The excitation field's polarization direction $E(t)$ is indicated by the arrow. **b**, Image changes as a function of time delay. The arrows indicate the polarization direction of the excitation fields. **c**, Phase map of the measured intensity oscillations for every position on the membrane. **d**, Illustration of how a travelling-wave excitation (red) produces converging and diverging electron trajectories (blue) of the attosecond pulse train. **e**, Illustration of the imaging geometry with an image plane slightly off the detector in order to observe positions and angles at the same time (differential phase contrast). **f**, Position-dependent intensity changes versus time in comparison with a trajectory simulation. **g**, Phase and delay across the sample (dots) in comparison with the simulation (blue). The travelling wave advances in space-time by $12 \mu\text{m}^{-1}$.

of the incoming electron packet (~ 0.5 eV). If these parameters are improved, even shorter electron pulses could be obtained, which might be useful to study electron–electron interactions on sub-attosecond timescales. While pulse trains may offer space–time access to cycle-reversible processes (for example, linear/nonlinear optics/plasmonics at atoms/molecules/nanostructures, Bloch oscillations, tunnelling in laser fields, cycle-induced macroscopic currents) or such with less than few-femtosecond time constants (for example, Auger decays, multi-electron ionization, damping in plasmonics), certain experiments on cycle-irreversible/slower dynamics or processes that cannot be multi-cycle excited due to damage (for example, dielectric breakdown, molecular dissociations) will require isolated electron pulses and not a pulse train. The reported concept offers several ways to do so. First, the incoming electron packet can be pre-compressed by terahertz radiation¹³ or other means to few-femtosecond duration (that is, short enough to inject it into a single cycle of the compression laser). Alternatively, optical single-cycle pulses can be used to deflect an isolated electron pulse out of the pulse train. It is also possible to filter out via single-cycle sideways deflection an attosecond electron pulse directly out of longer pulses or even out of a continuous beam. With compact multi-electron sources and/or sub-megahertz laser repetition rates (see Methods), about 10^6 – 10^8 electrons per second will impinge on the sample, enough for pump–probe experiments. Any future advances in source technology will directly apply.

Modern electron microscopy and diffraction have a huge application range and almost no sample-type or morphology restrictions. We therefore think that attosecond electron diffraction and microscopy may become a versatile alternative to conventional attosecond spectroscopy for visualizing fundamental light–matter interactions in space and time.

Methods

Methods, including statements of data availability and any associated accession codes and references, are available at <https://doi.org/10.1038/s41567-017-0007-6>.

Received: 27 July 2017; Accepted: 17 October 2017;
Published online: 27 November 2017

References

- Paul, P. M. et al. Observation of a train of attosecond pulses from high harmonic generation. *Science* **292**, 1689–1692 (2001).
- Hentschel, M. et al. Attosecond metrology. *Nature* **414**, 509–513 (2001).
- Kienberger, R. et al. Atomic transient recorder. *Nature* **427**, 817–821 (2004).
- Smirnova, O. et al. High harmonic interferometry of multi-electron dynamics in molecules. *Nature* **460**, 972–977 (2009).
- Sansone, G. et al. Electron localization following attosecond molecular photoionization. *Nature* **465**, 763–766 (2010).
- Lucchini, M. et al. Attosecond dynamical Franz-Keldysh effect in polycrystalline diamond. *Science* **353**, 916–919 (2016).
- Tao, Z. S. et al. Direct time-domain observation of attosecond final-state lifetimes in photoemission from solids. *Science* **353**, 62–67 (2016).
- Niikura, H. et al. Sub-laser-cycle electron pulses for probing molecular dynamics. *Nature* **417**, 917–922 (2002).
- Itatani, J. et al. Tomographic imaging of molecular orbitals. *Nature* **432**, 867–871 (2004).
- Blaga, C. I. et al. Imaging ultrafast molecular dynamics with laser-induced electron diffraction. *Nature* **483**, 194–197 (2012).
- Wolter, B. et al. Ultrafast electron diffraction imaging of bond breaking in di-ionized acetylene. *Science* **354**, 308–312 (2016).
- Schneider, W. et al. 800-fs, 330- μJ pulses from a 100-W regenerative Yb:YAG thin-disk amplifier at 300 kHz and THz generation in LiNbO₃. *Opt. Lett.* **39**, 6604–6607 (2014).
- Kealhofer, C. et al. All-optical control and metrology of electron pulses. *Science* **352**, 429–433 (2016).
- Kirchner, F. O., Gliserin, A., Krausz, F. & Baum, P. Laser streaking of free electrons at 25 keV. *Nat. Photonics* **8**, 52–57 (2014).
- Priebe, K. E. et al. Attosecond electron pulse trains and quantum state reconstruction in ultrafast transmission electron microscopy. Preprint at <https://arxiv.org/abs/1706.03680> (2017).
- Barwick, B., Flannigan, D. J. & Zewail, A. H. Photon-induced near-field electron microscopy. *Nature* **462**, 902–906 (2009).
- Baum, P. & Zewail, A. H. Attosecond electron pulses for 4D diffraction and microscopy. *Proc. Natl Acad. Sci. USA* **104**, 18409–18414 (2007).
- Sears, C. M. S. et al. Production and characterization of attosecond electron bunch trains. *Phys. Rev. Spec. Top. Accel. Beams* **11**, 061301 (2008).
- Feist, A. et al. Quantum coherent optical phase modulation in an ultrafast transmission electron microscope. *Nature* **521**, 200 (2015).
- Kozak, M. et al. Optical gating and streaking of free electrons with sub-optical cycle precision. *Nat. Commun.* **8**, 14342 (2017).
- Gliserin, A., Walbran, M., Krausz, F. & Baum, P. Sub-phonon-period compression of electron pulses for atomic diffraction. *Nat. Commun.* **6**, 8723 (2015).
- Engelen, W. J., van der Heijden, M. A., Bakker, D. J., Vredendregt, E. J. D. & Luiten, O. J. High-coherence electron bunches produced by femtosecond photoionization. *Nat. Commun.* **4**, 1693 (2013).

23. Shao, H. C. & Starace, A. F. Detecting electron motion in atoms and molecules. *Phys. Rev. Lett.* **105**, 263201 (2010).
24. Yakovlev, V. S., Stockman, M. I., Krausz, F. & P. Baum, P. Atomic-scale diffractive imaging of sub-cycle electron dynamics in condensed matter. *Sci. Rep.* **5**, 14581 (2015).
25. Stingl, J. et al. Electron transfer in a virtual quantum state of LiBH_4 induced by strong optical fields and mapped by femtosecond x-ray diffraction. *Phys. Rev. Lett.* **109**, 147402 (2012).
26. Morimoto, Y., Kanya, R. & Yamanouchi, K. Light-dressing effect in laser-assisted elastic electron scattering by Xe. *Phys. Rev. Lett.* **115**, 123201 (2015).
27. Cavalieri, A. L. et al. Attosecond spectroscopy in condensed matter. *Nature* **449**, 1029–1032 (2007).
28. Eckle, P. et al. Attosecond ionization and tunneling delay time measurements in helium. *Science* **322**, 1525–1529 (2008).
29. Schultze, M. et al. Delay in photoemission. *Science* **328**, 1658–1662 (2010).
30. Klunder, K. et al. Probing single-photon ionization on the attosecond time scale. *Phys. Rev. Lett.* **106**, 143002 (2011).
31. Neppl, S. et al. Direct observation of electron propagation and dielectric screening on the atomic length scale. *Nature* **517**, 342–346 (2015).
32. Ryabov, A. & Baum, P. Electron microscopy of electromagnetic waveforms. *Science* **353**, 374–377 (2016).

Acknowledgements

This work was supported by the European Research Council (grant DIVI) and the Munich-Centre for Advanced Photonics. Y.M. acknowledges support from a JSPS Postdoctoral Fellowship for Research Abroad. We thank B.-H. Chen and A. Ryabov for help with the laser, S. Stork for help with the foils and F. Krausz for awesome support and inspiring discussions.

Author contributions

Y.M. and P.B. conceived the experiment, Y.M. measured the data, Y.M. and P.B. evaluated the data and Y.M. and P.B. wrote the manuscript.

Competing interests

The authors declare no competing financial interests.

Additional information

Supplementary information is available for this paper at <https://doi.org/10.1038/s41567-017-0007-6>.

Reprints and permissions information is available at www.nature.com/reprints.

Correspondence and requests for materials should be addressed to P.B.

Publisher's note: Springer Nature remains neutral with regard to jurisdictional claims in published maps and institutional affiliations.

Methods

Experimental details. The experimental set-up is shown in Supplementary Fig. 1a. Electrons are emitted by two-photon photoemission³³ at a 50-kHz repetition rate from a 20-nm gold film and accelerated to 70 keV by a static voltage (Heinzinger GmbH). In the diffraction experiment, the beam is focused by the first magnetic lens (ML1) onto the detector (TVIPS GmbH) which are located ~0.7 m and ~1.3 m afar from the sample, respectively. In the microscopy experiment, ML1 is set to beam collimation and a second magnetic lens (ML2) provides a magnification of ~×6.55. The optical set-up (see Supplementary Fig. 1a) is an interferometer that produces a non-curved, parallel and stable optical wavefront of appropriate intensity at both foils over dimensions covering the entire electron beam diameter. We split the laser pulse into two replicas travelling at a beam diameter of < 1 mm in parallel with a distance of ~1.5 mm. The two beams are focused into the electron beam line by a common lens L1 ($f = 600$ mm) that is placed before the beamsplitter, so that the shape of the wavefront is nearly identical at the two electron–foil interactions. We set the two laser focal points slightly before the two foils to avoid different Gouy phase shifts and to make both wavefronts close to flat at the foils. The optical phase front sweeps over the finite electron beam profile in a sideways direction. The compressed electron pulses are therefore tilted with respect to their propagation direction, but this tilt is effectively compensated at the second foil, which is aligned in parallel to the first one by < 0.1°. If non-tilted electron pulses are needed, velocity matching can be applied¹⁴ to produce equal timing differences of the optical phase front and the electron incidence along the entire membrane surface. The longitudinal length over which the electron pulses keep compressed (depth of focus) is hundreds of micrometres, which well covers the thickness of samples in electron diffraction or microscopy.

Optical overlap in time. The modulation and excitation laser pulses were stretched to ~1.7-ps duration with a grating sequence, in order to cover the entire electron pulses (~1 ps) in time. Scanning the delay between the two pulses reveals whether this stretching is sufficient. Supplementary Fig. 1b shows the delay dependence of the streaking deflectogram's contrast, which is evaluated by the amplitude of the centre-of-mass oscillation. The offset of ~10 % is due to noise that seemingly produces an amplitude even without real deflection. The width of this cross-correlation trace (black curve) is 2.4 ps (full-width at half-maximum), which is close to the expected value of 2.2 ps given by convolution of the laser pulse duration (~1.7 ps), the electron pulse duration (~1 ps) and the velocity mismatch effect on the sample (~1 ps). This result demonstrates that all electrons feel almost identical optical cycles of the laser field over their entire 1-ps duration.

Interferometric stability and long-term drift correction. The optical set-up was constructed with the best available optomechanics and with very rigid and optimized mechanical adapters. Attosecond-precision phase delay is created via a motorized tilt of a 1-mm-thick fused-silica plate in one of the beams. We continuously monitor with an auxiliary beam camera the phase delay in real time (1 Hz) by using an interferometric technique³⁴. The fast jitter (1 Hz to 50 kHz) has an upper limit of < 400 as (evaluated from fringe visibility) and the optical set-up drifts by less than 50 as per 10 min. In experiments requiring longer averaging times, we scanned the pump–probe delay many times rapidly over a range covering two laser cycles with 30 steps. After the complete measurement (many scans), we analysed the phase of the centre-of-mass oscillation for each scan by Fourier analysis and sorted the data accordingly, in order to cancel out slow drifts of the phase, which can occur from slow mechanical drifts of the interferometer, from drift of the kinetic energy of the electron beam (most probable) and from thermal expansions or slow movements of the Si and Si₃N₄ foils in the vacuum chamber. Note that our evaluations of potential delays of diffraction are not affected by such a procedure, because the direct beam and the Bragg spots were recorded in identical image sequences and therefore corrected together.

Foils. The compression membrane is a 50-nm-thick, 5 × 5 mm² large amorphous Si₃N₄ foil (Norcada Inc.). To prevent electrostatic charging in the electron beam, the front side is coated with ~5 nm aluminium except at the region where the electrons and laser cross. The streaking, diffraction and microscopy sample is a 60-nm-thick, 0.15 × 0.15 mm² large single-crystalline silicon foil in the (100) orientation (Norcada Inc.) and coated with an additional SiN/SiO layer that flattens the membrane. The crystalline quality of the silicon foil is close to perfect; all Bragg spots are almost as sharp as the direct beam and rocking curve widths are less than 1° (see Fig. 3b).

Electron flux and signal-to-noise ratio estimation. The electron source applied in this study provided 1-ps pulses with a current of ~1 electron per pulse at 130 μm beam diameter, which was enough to observe 1% Bragg intensity changes within 100-s integration time. State-of-the-art dense-pulse electron sources^{35,36} provide ~1,000 electrons in a 100-μm-diameter beam at ~100 fs pulse duration (that is, a peak current 10⁴ times higher than in our experiment). Due to the velocity-matching geometry at the dielectric foils, such brightness will more or less directly convert to the attosecond pulse train; losses occur only from the temporal background and from foil absorptions. Some Coulomb repulsion can probably be tolerated, because the beam is large and the temporal focus is only millimetres

apart, so there will not be much time for space-charge dynamics to build up³⁷. We expect ~10 electrons per individual attosecond pulse, or roughly 10⁷–10⁸ electrons per second at 50–500-kHz repetition rate. This current is enough for pump–probe diffraction or microscopy of reasonably good-quality samples^{35,36,38}. If a single isolated attosecond electron pulse is generated by single-optical-cycle filtering (see main text), we still can expect 10⁵–10⁷ electrons per second. Terahertz-driven or microwave-driven pre-compression^{13,21} can improve this value down to the limits given by the space-charge regime³⁷, to be clarified by simulations, or alternatively reduce the demands on the electron source.

Dependence of compression and deflection on the experimental angle combinations. Supplementary Fig. 1d shows a simulation of the amplitude of the longitudinal compression and the sideways deflection as a function of the laser–electron and laser–foil angles in an experiment. Finite-difference-time-domain simulations (Lumerical Inc.) with ~8 grid points inside the membrane were used to obtain the space-time electromagnetic fields. Classical particle-tracking simulations delivered the final velocity change $\Delta v/v_0$ as a function of the optical phase. The resulting amplitudes show that certain angle combinations can optimize compression, deflection or both. The white lines denote impractical angles, where, for example, the electrons would pass in grazing incidence to the membrane. The experimental conditions are marked by the black dotted cross. The predicted location of the temporal focus at these angles is at 4.1 mm distance, which compares well to the 3.7 mm of the experiment. The shorter dotted line indicates another useful condition where there is purely an efficient compression but no deflection.

Streaking deflectogram simulation. The deflectogram $D(x, \Delta t)$, that is, the spatial beam profile integrated along the non-streaked direction as a function of delay, can be simulated by

$$D(x, \Delta t) = \int_{-\frac{\pi}{\omega}}^{\frac{\pi}{\omega}} I_{el}(t) P(x - \alpha(t)L) dt \quad (1)$$

with the time-dependent deflection $\alpha(t) = \alpha_0 \cos(\omega(t - \Delta t))$, where x is the position on the detector, Δt is the delay between the electron pulse and the deflecting field, ω is the angular frequency of the laser field, L is the sample–detector distance, $I_{el}(t)$ is the temporal shape of the electron pulse, and $P(x)$ is the intensity distribution of electrons on the detector without the deflecting field. To determine the pulse duration by the fit, we model $I_{el}(t)$ by a Gauss function, $I_{el}(t) = I_{as} \exp(-\frac{1}{2}t^2/\tau_d^2) + I_{BG}$, where τ_d is the pulse duration and I_{as} and I_{BG} represent the intensity of the compressed and un-compressed electrons, respectively.

Delay analysis. The delays of the Bragg spots are determined by computing the periodic oscillation of the deflectogram's time-dependent displacement with a centre-of-mass analysis and fitting a sinusoidal temporal phase. This procedure, which is related to those used commonly in attosecond laser spectroscopy^{27,31}, requires no assumptions and delay evaluation is robust, because each Bragg spot and the direct beam are measured simultaneously. Alternatively, we also applied the deflectogram fitting procedure using equation (1) for each pair of Bragg spot and direct beam, and obtained from the differences of the fitted phases the delays (open circles in Fig. 3f).

Laser-driven electronic motion in silicon. Bragg spot intensity is related to the scattering potential via the structure factor and a time-resolved recording of Bragg spots from a material under laser excitation can therefore reveal time-dependent charge-density maps^{23–26}. Here we estimate the magnitude of Bragg intensity changes originating from atomic-scale electronic motion in silicon. Via density functional theory³⁹, we calculate in the limit of an electrostatic field the valence charge densities in Si with and without the electric field and take the difference between them. Static fields seem appropriate for a rough estimation because the optical frequency is far away from any resonances of the refractive index. Inner electrons are assumed to be screened from the field. Supplementary Fig. 1c shows the change of electron density in silicon as seen by the electron beam in the experiment along $[-1/\sqrt{2}, \sqrt{2}, 1/\sqrt{2}]$ for an electric field of 6×10^9 V m⁻¹, which is achievable with single-cycle excitation pulses⁴⁰. The polarization direction of the electric field is the same as in the experiment (see Supplementary Fig. 1a). Diffraction is calculated with the help of the first Born approximation from the scattering potential according to the charge motion. The predicted intensity changes of the $1\bar{1}\bar{3}$, 311 , $1\bar{1}\bar{3}$ and $\bar{3}11$ reflections have an amplitude of ~0.3%, which is on the same order of magnitude as the signal-to-noise ratio in the experiment (see Fig. 3c). Silicon's response to electric fields is limited by the mono-atomic composition and the equal polarizability of all Si–Si bonds. Materials with optical resonances such as graphene or ionic crystals can have Bragg spot changes of several per cent^{24,25} and are therefore better suited for a proof-of-principle experiment on charge-density mapping with our attosecond pulses²⁵. Attosecond diffraction should also be possible in grazing-incidence reflection geometry for studying bulk crystals or surfaces, provided that the optical excitation speed is velocity-matched (for example, with a laser beam propagating within the

substrate) or quasi-phase-matched (for example, by surface nanostructuring). It is also possible to apply scanning electron microscopy to directly probe the inter-atomic fields in real space^{41,42}. This approach may be insensitive to inner-electron scattering and therefore useful for studying electron dynamics in heavy-element materials that may produce too much static background in diffraction²⁴.

Attosecond electron microscopy simulations. To understand the measured attosecond microscopy images, we invoke a ray-optical simulation approach. We assume a homogeneous, collimated illumination and a time-dependent, local deflection at each point. From the position and angle of each electron after the sample, its final position on the screen is determined with the help of a transfer matrix, which represents the focusing effect of the magnetic lens system and the free-space propagations. Integration over all trajectories produces the simulated distortion image. Spatial resolution is in the experiment deteriorated by the angular distribution of the incoming electrons on the sample due to the finite emittance, by aberrations of the magnetic lens and by the point spread function of the detector ($\sim 30\ \mu\text{m}$ root-mean-square). We therefore convolute the projected image with a Gauss function whose width corresponds to the observed resolution of the direct beam ($60\ \mu\text{m}$ root-mean-square on the screen). The travelling-wave excitation in the experiment is modelled by a phase delay that is linear to the sample position, that is, $a(x, t) = a_0 \cos(\omega t - \phi_x x)$, where ϕ_x is the wavefront tilt parameter. This procedure produces the simulation results plotted in Fig. 4f, in noteworthy agreement with the experiment.

Integration into a commercial electron microscope. Here we consider how our dielectrics-based pulse compression and metrology concepts could be integrated into a commercial electron microscope as also possible with graphite membranes¹⁵. Due to the short compressor-to-sample distance that is offered by our dielectric foils (only 4 mm in the experiment and potentially less with higher laser fields), it should be possible to set the microscope to collimated-beam illumination and place the compressor stage right in front of the sample within the objective-lens region¹⁵. Typically there are several millimetres of space between the twin-lens elements. Assuming 120-keV electron energy, a residual divergence of $10\ \mu\text{rad}$ in the beam and a 45° incidence of the lasers, geometrical considerations predict a smearing of the temporal resolution by roughly 200 as, which seems acceptable. Alternatively, the compressor stage can be placed before the objective lens, for example at the location of a condenser aperture or bi-prism mount, if temporal distortions of the magnetic imaging are properly considered⁴³ and optimized⁴⁴.

Pulse trains versus isolated pulses and diffraction versus microscopy. Here we consider to what extent attosecond electron pulse trains are useful for space–time investigations or whether isolated pulses would be required. With pulse trains and diffraction, one can directly record only such space–time dynamics that is the same in each optical pump cycle. Fortunately, this few-femtosecond reversibility seems frequently available in attosecond physics. For example, photoemission takes less than hundreds of attoseconds^{7,27,30,31}. Auger decays have few-femtosecond time constants^{45,46}, laser-driven interband/intraband Bloch oscillations^{47–49} occur within each optical cycle, all linear and nonlinear optical effects (for example, second/third/higher-harmonic generation)^{49–52} involve cycle-reversible atomic-scale charge-density displacements⁵⁴ and macroscopic currents in dielectrics can be initiated and controlled on sub-cycle timescales^{53,54}. Recombination might also be ultrafast in a condensed-matter environment. Ultrafast electron-energy loss by plasmons⁵⁵ or inner-shell core-loss processes⁵⁶ may also be expected to reversibly depend on the presence of light cycles. In contrast, isolated attosecond electron pulses will be required for studying cycle-irreversible dynamics (for example, long-lived electron correlations, heating, avalanche ionization and molecular dissociations), or processes that cannot be multi-cycle excited due to damage (for example, dielectric breakdown and extreme strong-field phenomena). The time–energy correlations that are created in the electron pulses with our concept might be useful for electron spectroscopy, for example via phase-space rotation^{57,58}. Real-space attosecond microscopy can be invoked to image, for example, the oscillating electromagnetic fields⁵² that cause the function of metamaterials or nanophotonic circuitry.

Data availability. Data that support the plots within this paper and other findings of this study are available from the corresponding author upon reasonable request.

References

- Kasmi, L., Kreier, D., Bradler, M., Riedle, E. & Baum, P. Femtosecond single-electron pulses generated by two-photon photoemission close to the work function. *New J. Phys.* **17**, 033008 (2015).
- Baum, P., Lochbrunner, S., Piel, J. & Riedle, E. Phase-coherent generation of tunable visible femtosecond pulses. *Opt. Lett.* **28**, 185 (2003).
- Waldecker, L., Bertoni, R. & Ernstorfer, R. Compact femtosecond electron diffractometer with 100 keV electron bunches approaching the single-electron pulse duration limit. *J. Appl. Phys.* **117**, 044903 (2015).
- Gerbig, C., Senfleben, A., Morgenstern, S., Sarpe, C. & Baumert, T. Spatio-temporal resolution studies on a highly compact ultrafast electron diffractometer. *New J. Phys.* **17**, 043050 (2015).
- Baum, P. & Zewail, A. H. 4D attosecond imaging with free electrons: Diffraction methods and potential applications. *Chem. Phys.* **366**, 2–8 (2009).
- Lahme, S., Kealhofer, C., Krausz, F. & Baum, P. Femtosecond single-electron diffraction. *Struct. Dyn.* **1**, 034303 (2014).
- Gonze, X. et al. ABINIT: First-principles approach to material and nanosystem properties. *Comput. Phys. Commun.* **180**, 2582–2615 (2009).
- Schultze, M. et al. Attosecond band-gap dynamics in silicon. *Science* **346**, 1348–1352 (2014).
- Shibata, N. et al. Differential phase-contrast microscopy at atomic resolution. *Nat. Phys.* **8**, 611–615 (2012).
- Mueller, K. et al. Atomic electric fields revealed by a quantum mechanical approach to electron picodiffraction. *Nat. Commun.* **5**, 5653 (2014).
- Weninger, C. & Baum, P. Temporal distortions in magnetic lenses. *Ultramicroscopy* **113**, 145–151 (2012).
- Kreier, D., Sabonis, D. & Baum, P. Alignment of magnetic solenoid lenses for minimizing temporal distortions. *J. Optics* **16**, 075201 (2014).
- Drescher, M. et al. Time-resolved atomic inner-shell spectroscopy. *Nature* **419**, 803–807 (2002).
- Reckenthaeler, P. et al. Proposed method for measuring the duration of electron pulses by attosecond streaking. *Phys. Rev. A* **77**, 042902 (2008).
- Garg, M. et al. Multi-petahertz electronic metrology. *Nature* **538**, 359–363 (2016).
- Mashiko, H., Oguri, K., Yamaguchi, T., Suda, A. & Gotoh, H. Petahertz optical drive with wide-bandgap semiconductor. *Nat. Phys.* **12**, 741–745 (2016).
- Hohenleutner, M. et al. Real-time observation of interfering crystal electrons in high-harmonic generation. *Nature* **523**, 572 (2015).
- Vampa, G. et al. Linking high harmonics from gases and solids. *Nature* **522**, 462 (2015).
- Luu, T. T. et al. Extreme ultraviolet high-harmonic spectroscopy of solids. *Nature* **521**, 498–502 (2015).
- Ndabashimiye, G. et al. Solid-state harmonics beyond the atomic limit. *Nature* **534**, 520 (2016).
- Schiffrin, A. et al. Optical-field-induced current in dielectrics. *Nature* **493**, 70–74 (2013).
- Schultze, M. et al. Controlling dielectrics with the electric field of light. *Nature* **493**, 75–78 (2013).
- Carbone, F., Kwon, O.-H. & Zewail, A. H. Dynamics of chemical bonding mapped by energy-resolved 4D electron microscopy. *Science* **325**, 181–184 (2009).
- van der Veen, R. M., Penfold, T. J. & Zewail, A. H. Ultrafast core-loss spectroscopy in four-dimensional electron microscopy. *Struct. Dyn.* **2**, 024302 (2015).
- Verhoeven, W. et al. Time-of-flight electron energy loss spectroscopy using tm110 deflection cavities. *Struct. Dyn.* **3**, 054303 (2016).
- Zhou, F., Williams, J. & Ruan, C.-Y. Femtosecond electron spectroscopy in an electron microscope with high brightness beams. *Chem. Phys. Lett.* **683**, 488–494 (2017).